Tuning CO_2 Methanation Selectivity via MgO/Ni Interfacial Sites

*Yufei Xie [a], Valentijn De Coster [a], Lukas Buelens [a], Hilde Poelman [a], Bensu Tunca [b], Jin-Won Seo [b], Christophe Detavernier [c] and Vladimir Galvita [a,]**

[a] Laboratory for Chemical Technology, Ghent University, Tech Lane Ghent Science Park A 125, B-9052 Ghent, Belgium

[b] Department of Materials Engineering, KU Leuven, Kasteelpark Arenberg 44, B-3001 Leuven, Belgium

[c] Department of Solid State Sciences, Ghent University, Krijgslaan 281, S1, B-9000 Ghent, Belgium

* Corresponding author: Vladimir Galvita, Vladimir.Galvita@UGent.be

ABSTRACT: CO_2 methanation is a promising carbon-neutral process to produce synthetic natural gas. Ni is a cost-effective catalyst, but needs improved selectivity to compete with noble metal catalysts. Herein, MgO-promoted Ni/SiO_2 is investigated as model system and compared to unpromoted Ni/SiO_2. The catalysts are characterized with chemisorption, transmission electron microscopy and *in situ* quick X-ray absorption spectroscopy. After reduction, MgO partly covers metallic Ni forming an MgO/Ni interface, which proves to be critical to the reaction through metal oxide-metal interaction. Combining kinetic and *in situ* diffuse reflectance infrared Fourier transform spectroscopy, formyl group hydrogenation was found to be the rate determining step for both catalysts. The enhanced CH_4 selectivity after MgO addition is attributed to facilitated conversion of the key intermediates - formyl groups - due to a lower energy barrier. This work provides unambiguous experimental proof for the role of the MgO/Ni interface in the reactivity for CO_2 methanation.

KEYWORDS: Ni-based catalyst, MgO promotion, MgO/Ni interface, formyl group intermediate.

1. INTRODUCTION

Methanation is a promising technology to catalytically convert CO_2 into CH_4, ideally utilizing renewable H_2[1, 2]. The product, synthetic natural gas, can not only be injected directly into the gas grid, but also reduces the exploitation and usage of untapped crude fossil fuels. On the other hand, the intermittency of renewable energy makes it hard to directly charge solar or wind power electricity into electric grids, while H_2 produced from electrolysis is too costly to store and transport. However, converting green H_2 into CH_4 through methanation can be applied as an efficient energy storage method[3-5]. In order to achieve this power conversion, understanding the methanation process is of the essence. Moreover, together with the reverse water gas shift reaction (RWGS), it constitutes an important element in many other CO_2 conversion routes.

The heart of a catalytic process is an efficient catalyst. So far, catalytic research on CO_2 methanation has focused on the use of Ni[6-9], Ru[10, 11], Rh[12, 13], Pd[14, 15] and Co[16, 17] as active metal. Among these, noble metals exhibit extraordinary CO_2 activation ability at low temperature. On the other hand, to reduce the usage of noble metals and the associated cost, transition metal Ni with moderate performance, but much lower price is a viable option[18]. However, for industrial application, it is necessary to develop a Ni-based catalyst with high CO_2 conversion and CH_4 selectivity.

Methanation performance is not only influenced by the active metal, but also the support, promoter and preparation conditions are important to obtain a catalyst that demonstrates high selectivity and activity[19-22]. Typical supports for methanation catalysts are metal oxides with high surface area, e.g. Al_2O_3[23], SiO_2[24], CeO_2[25, 26] or TiO_2[27]. These supports also influence the activity of the catalytic metals mentioned above, indicating that they are often not inert and their interaction with the catalyst nanoparticles gives rise to new phenomena at the interface such as metal-support interaction (MSI)[19, 28]. Typical MSI phenomena relate to the interfacial perimeter, nanoparticle morphology, charge transfer, chemical composition and encapsulation, also termed strong metal-support interaction[12, 26, 29]. A promoter added to the support or as a decoration over catalytic nanoparticles can further create new specific interfacial active sites or adjust the electronic state of the active element[30]. Either way, the type of support or presence of a promoter can critically alter the catalytic performance and reaction mechanism through mediation of the interface, hence, in order to optimize performance, strategies for controlling this type of interactions are desirable.

Among possible Ni promoters, MgO has shown importance in different kinds of reaction, like reforming and methanation[31, 32]. The basicity of MgO is suitable for CO_2 activation, as it shows a good adsorption ability for CO_2[33]. In addition, due to the same face-centered cubic crystal structure and almost identical atomic size (Ni^{2+}: 69 pm; Mg^{2+}: 72 pm), MgO and NiO interact easily with each other, yielding e.g. small promoted Ni particles, even Ni single atoms, or solid solutions[34, 35].

While MgO has already been utilized to enhance the performance of Ni-based catalysts, the structure of these promoted catalysts as well as the exact reaction mechanism are not well resolved, even though these are critical to describe the promotion effect. Possible reaction pathways for methanation are shown in Scheme 1, which are classified according to whether CO serve as a intermediate[4, 36]. For indirect pathway, CO* is first produced through RWGS. Afterwards, CO* either desorb forming CO(g) or further hydrogenate proceed three different routes, *COH, HCO* or C*, leading to the formation of CH_4. For direct pathway, methanation starts through H-assist transformation, producing HCOO* without going through CO*.

In a theoretical investigation, the H mediated pathway via HCOO* was found to be the primary route on Ni(111)/MgO(110). MgO contributes to the removal of OH* and H_2O formation[37]. However, in several other density functional theory (DFT) calculations[38, 39], as well as through ambient-pressure X-ray photoelectron spectroscopy (AP-XPS) investigations[6], CO formation via CO_2 direct dissociation, followed by carbon hydrogenation, is validated to be energetically favorable on Ni(111).

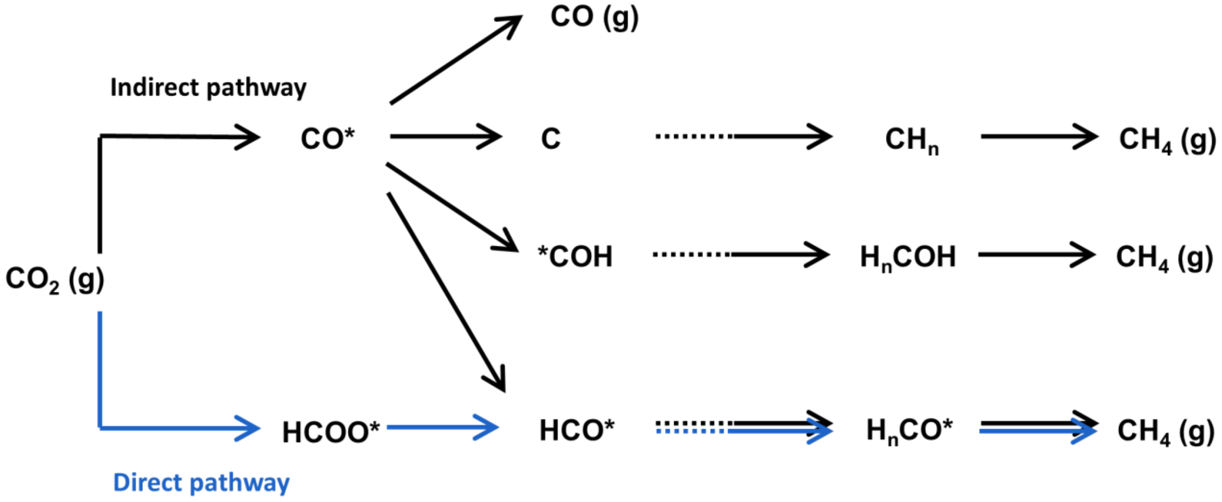

Scheme 1. Possible reaction pathways for CO_2 hydrogenation. Black: indirect pathway; Blue: direct pathway.

In non-model systems, the reaction mechanism is a matter of debate, especially when promoters are included. Park et al.[40] ascribed the promotion effect of MgO to the formation of $MgOCO_2$. Several reports proposed similar viewpoints on Ni-based catalysts, in that MgO enhances the adsorption capacity of CO_2 and its subsequent conversion[33]. On the other hand, more research concluded that the rate determining step is the conversion of key intermediates like CO* or HCOO*, other than CO_2 adsorption. For instance, Hongmanorom and co-workers[41] found that base sites resulting from MgO addition promote the formation of monodentate formate, which is more active for conversion towards CH_4 than bidentate formate. In other work, the CO adsorption strength is considered as the main descriptor, when H_2 assisted CO dissociation is claimed as the rate determining step[42, 43].

As demonstrated by the abovementioned literature, the promotion of Ni methanation catalysts by MgO holds promise, yet lacks knowledge regarding the interaction between MgO and Ni. To advance the understanding of how MgO affects the performance of Ni during CO_2 methanation, a set of MgO/Ni/SiO_2 catalysts with 15wt.% Ni loading and varying MgO promotion (0-3wt.%) has been studied. SiO_2, which has little interaction with Ni and MgO, is selected as support in order to focus on Ni itself and the Ni-MgO interaction. Controlled catalytic performance and kinetic parameter tests provide insight into the reaction network. By combining kinetic testing with *in situ* steady-state and transient measurements, the effect of MgO is determined at a mechanistic level. The reaction tests are combined with chemisorption characterization, scanning transmission electron microscopy (STEM), *in situ* quick X-ray absorption spectroscopy (QXAS), as well as *in situ* transient diffuse reflectance infrared Fourier Transform spectroscopy (DRIFTS), to identify the structure and surface of the catalyst under realistic conditions.

2. EXPERIMENTAL

2.1 Catalyst Synthesis

Ni supported on SiO_2 with varying Ni loadings was prepared by incipient wetness impregnation to obtain different particle sizes. Typically, a proper amount of $Ni(NO_3)_2{\cdot}6H_2O$ (99.999%, Sigma-Aldrich) was dissolved in deionized water. The solution was added dropwise to amorphous SiO_2

(99.5%, Sigma-Aldrich). Afterwards, the sample was dried at 120 °C overnight, ground and calcined at 600 °C for 2 h. The catalysts are labeled as xNiSi (x=0.5, 2, 5, 15) where x stands for the weight percentage of Ni (metal base, e.g. 15NiSi stands for 15 wt.% Ni supported on SiO_2).

MgO-added samples were prepared by sequential incipient wetness impregnation for one Ni loading. First, one batch of 15NiSi was prepared using the method mentioned above. Then, a proper amount of $Mg(NO_3)_2·6H_2O$ (Sigma-Aldrich, ≥ 99.0%) dissolved in deionized water was added dropwisely. The samples were dried at 120 °C overnight, ground and calcined at 600 °C for 2 h. These catalysts are labeled as xMg15NiSi (x=0, 0.1, 0.3, 0.5, 1, 1.5, 3) where x stands for the weight percentage of Mg (metal base). For comparison, 1 wt.% Mg supported on SiO_2 without Ni, labeled as 1Mg0NiSi, was also prepared by the same method. The state after synthesis is denoted “as-prepared”.

2.2 Catalyst Characterization

N_2 physisorption-desorption experiments were carried out in a Micromeritics Tristar 3000 analyzer at -196 °C. The specific surface area (SSA) of the samples was calculated by means of the Brunauer−Emmett−Teller (BET) method.

Powder X-ray diffraction (XRD) analyses were performed on reduced samples using a Siemens Diffractometer Kristalloflex D5000 (Cu Kα radiation, $\lambda = 0.154$ nm). The crystallite size of Ni was calculated by means of the Scherrer equation.

Temperature programmed experiments, comprising H_2 reduction (H_2-TPR), H_2 chemisorption, CO dissociation (TP-CO dissociation), C hydrogenation (C-TPH), were conducted in a Micromeritics AutoChem II chemisorption analyzer. Typically, 100 mg of sample was used for one test.

For H_2-TPR, the sample was pretreated in Ar (60 mL/min) at 600 °C for 30 min and cooled down to 50 °C. Then, the sample was heated to 600 °C with a rate of 10 °C/min, maintaining that temperature for 30 min, then resuming heating up to 900 °C with the same rate and again maintaining for 30 min in 5 vol.% H_2/Ar (60 mL/min). The reduction degree was calculated as in equation (1).

$$Reduction\ degree = \frac{measured\ H_2\ consumption}{theoretical\ H_2\ consumption} \times 100\% \qquad (1)$$

For H_2 chemisorption, the sample was first reduced at 600 °C for 30 min in 5 vol.% H_2/Ar (60 mL/min). Then, the gas was switched to pure Ar (60 mL/min) purging for 30 min in order to remove adsorbed H_2. After cooling down to 50 °C, 5 vol.% H_2/Ar was pulsed over the catalyst until the peak area detected at the outlet became constant. The surface area of metallic Ni was then calculated under the assumption that one Ni atom adsorbs one H atom.

For TP-CO dissociation, the sample was first reduced at 600 °C for 30 min in 5 vol.% H_2/Ar (60 mL/min). The gas was then switched to pure He (60 mL/min) for 30 min purging in order to remove adsorbed H_2. After cooling down to 50 °C, the gas was changed to 10 vol.% CO/He. Finally, the sample was heated to 600 °C at 10 °C/min. MS was used to detect the signal of CO_2 (m/z=44).

For C-TPH, the sample was first reduced at 600 °C for 30 min in 5 vol.% H_2/Ar (60 mL/min). Then, the gas was switched to pure He (60 mL/min) for 30 min to remove adsorbed H_2. After cooling down to 350 °C, 10 vol.% CO/He (60 mL/min) was introduced into the reactor for 30 min. Sequentially, the sample was cooled down to 50 °C in He and purged for 1 h. Finally, the sample was heated to 600 °C at a rate of 10 °C/min in 5 vol.% H_2/Ar (60 mL/min), while following the outlet with MS.

CO_2+H_2 and CO+H_2 temperature programmed surface reaction (CO_2+H_2 TPSR and CO+H_2 TPSR) experiments were carried out in a quartz fixed-bed reactor equipped with MS to detect products (CO_2 at m/z=44, CO at m/z=28, CH_4 at m/z=15, H_2 at m/z=2). The sample was first reduced at 600 °C for 30 min in a H_2/Ar mixture (90 mL/min, H_2:Ar=4:5). After cooling down to room temperature (RT), the gas was switched to CO_2:H_2:Ar=1:4:5 (or CO:H_2:He=0.05:4:5 for CO+H_2 TPSR) and the sample was heated to 350 °C at a rate of 10 °C/min.

In situ CO-DRIFTS and CO_2+H_2 DRIFTS were conducted with a Bruker Tensor 27 spectrometer, equipped with a cell with gas feed connections and resistive heating and a mercury–cadmium–telluride (MCT) detector. Typically, the sample diluted with KBr (1:20) was placed into the DRIFTS cell, reduced at 500 °C for 1 h in H_2/He (90 mL/min, H_2:He=4:5). The maximum temperature that the DRIFTS setup can reach is 500°C. However, from H_2-TPR it follows that all Ni is reduced at this temperature. For CO-DRIFTS, the gas was then switched to He (50 mL/min) for 30 min to purge out all H_2. Afterwards, the sample was cooled down to 30 °C and 1% CO/He was introduced into the cell for 30 min. Finally, the gas was switched back to He and purged for 1 h. Spectra were recorded during exposure to 1% CO/He and under the He purge. For *in situ* DRIFTS, the diluted sample was reduced at 500 °C for 1 h in H_2/He (90 mL/min, H_2:He=4:5) and cooled down to 350 °C. Then, CO_2 (10 mL/min) was introduced for 30 min reaction, followed by switching the gas feed to H_2/He (90 mL/min, H_2:He=4:5), which was kept for 30 min. All spectra were collected with a resolution of 4 cm^{-1}. For each spectrum, 64 scans were measured.

High-angle annular dark-field (HAADF) scanning transmission electron microscopy (STEM) and energy dispersive X-ray (EDX) analysis were performed using a JEOL ARM200F probe-corrected microscope, operated at 200 kV and equipped with a cold-field emission gun and the large-angle SDD-EDX detector (Centurio, JEOL), to determine the elemental distribution within the reduced samples. TEM samples were prepared by placing a droplet of the colloidal dispersion of the sample in isopropanol on a holey carbon-coated copper grid.

Bright field scanning transmission electron microscopy (STEM), conducted using a JEOL JEM-2200FS, Cs-corrected microscope operated at 200 kV, was used to determine the particle size distribution of reduced samples. For each sample, a Lacey formvar/carbon film supported on a 200 mesh copper grid was immersed in the sample powder. After several minutes of contact time with the powder, the grid was removed and redundant powder was blown off before loading the grid into the microscope specimen holder.

QXAS measurements were performed at the ROCK beamline[44, 45] of the French synchrotron SOLEIL. The storage ring was operated at 2.75 GeV with a ring current of 450 mA in top-up mode. A Si(111) monochromator[46], oscillating at 2 Hz, scanned the Ni K-edge (8333 eV), covering both X-ray absorption near edge structure (XANES) and extended X-ray absorption fine edge structure (EXAFS) regions in one scan (energy range: 8150–8970 eV). Calibration was assured through the measurement of a Ni foil.

In situ QXAS measurements were conducted for 0Mg15NiSi and 3Mg15NiSi. For this purpose, both materials were ground to powders and 50% diluted with boron nitride. A 5 mm long catalyst bed was inserted in between two quartz wool plugs into a quartz capillary with an outer diameter of 1.2 mm (wall thickness: 0.010 mm, length: 115 mm). The capillary was mounted in a dedicated frame which was connected to gas feed lines through Swagelok fittings. This capillary reactor cell was positioned in a custom-built radiative heating furnace to reach desired reaction temperatures[44]. The inlet gas flow rates were maintained by means of calibrated Brooks mass flow controllers. A total flow rate of 7 mL/min was employed for all experiments.

Spectra were collected at RT under He for the as-prepared state of both catalysts. For *in situ* H_2-TPR QXAS, 3.2 mL/min H_2 mixed with 3.8 mL/min He was introduced into the system. The catalyst was then heated up to 600 °C, with 10 °C/min heating rate and a holding time of 30 min. After reduction, *in situ* CO_2 methanation QXAS is conduced. The reactor was cooled down to 350 °C. Then, CO_2 was introduced with a flow switching between 0.8 and 3.2 mL/min, together with a constant H_2 flow of 3.2 mL/min (CO_2:H_2 ratio of 0.25 and 1, respectively, balanced with He for a total flow of 7 mL/min). For the purpose of conducting *in situ* CO_2 oxidation QXAS, 3.2 mL/min CO_2 mixed with 3.8 mL/min He was introduced to the reduced sample at 600 °C.

In situ QXAS spectra were averaged over 10 consecutive scans to increase the signal-to-noise ratio. This resulted in a net time resolution of 5 s/spectrum. In case of *in situ* RT and *ex situ* reference measurements, 1000 spectra were averaged to maximize the data quality for EXAFS modeling. All averaged data were normalized and aligned using a dedicated Python normalization GUI[47].

EXAFS data analysis of RT XAS data was performed using the Athena and Artemis software packages[48]. Model structures of zero-valent Ni and Ni oxides were used to fit the Fourier transformed EXAFS (FT-EXAFS) data in R-space to derive quantitative structural parameters, namely: bond distance (R), coordination number (CN), Debye-Waller factor (DWF), amplitude reduction factor (S_0^2) and energy shift (ΔE_0).

All EXAFS data were fitted in the range R = 1–3.2 Å and k = 3–12.7 $Å^{-1}$. The value for S_0^2, as determined by fitting a Ni foil reference, was set to 0.90 for all EXAFS analyses. A common value for ΔE_0 was used for all scattering paths in a specific EXAFS dataset. Scattering paths for Ni-O and Ni-Ni were obtained from reference models of metallic Ni and NiO. The goodness of fit to the FT-EXAFS data in R-space was evaluated through the residual "R-factor" and the reduced chi square value (χ_v^2)[48].

To quantify the Ni reduction kinetics during H_2-TPR, multivariate curve resolution-alternating least squares (MCR-ALS) was performed considering 2 components. For this MCR-ALS analysis, the MATLAB® toolbox developed by Jaumot et al.[49] was applied, making use of the full recorded XAS energy range. Constraints for positivity of the concentrations and spectra were imposed, as well as equating the sum of all concentrations to 1. Initial estimates of the spectral type were provided via the toolbox's built-in PURE estimation method[50], with a 10% allowance of noise contribution. The quality of the MCR-ALS analysis was assessed via three goodness of fit parameters, as defined in literature[49, 50]: the percentage lack of fit relative to the experimental data (LOF), the percentage of explained data variance (R^2) and the standard deviation of residuals with respect to the experimental data (σ).

2.3 Catalytic Performance Test

Catalytic performance tests were carried out in a quartz fixed-bed reactor (7 mm inner diameter). For each experiment, 100 mg catalyst (100-200 μm) diluted with α-Al_2O_3 (catalyst:α-Al_2O_3 = 1:5) was loaded into the reactor. A K-type thermocouple was used to monitor the temperature of the catalyst bed. The sample was first heated in H_2/Ar (H_2:Ar = 4:5, total flow = 180 mL/min) to 600 °C (10 °C/min), maintained for 30 min, then cooled down to 350 °C. Subsequently, the gas was switched to CO_2:H_2:Ar (CO_2:H_2:Ar = 1:4:5, total flow = 200 mL/min) for reaction. Products were analyzed with an online Gas Chromatograph (GC, ThermoFisher Scientific, Trace 1310), equipped with a thermal conductivity detector (TCD) and a Molsieve 5A column and Hayesep-N column, using He as carrier gas. The conversion of CO_2 and selectivity to CH_4 and CO are calculated as follows:

$$CO_2 \text{ Conversion} = \frac{F_{CO2,in} - F_{CO2,out}}{F_{CO2,in}} \times 100\% \tag{2}$$

$$CH_4 \text{ Selectivity} = \frac{F_{CH4,out}}{F_{CH4,out} + F_{CO,out}} \times 100\% \tag{3}$$

$$CO \text{ Selectivity} = \frac{F_{CO,out}}{F_{CH4,out} + F_{CO,out}} \times 100\% \tag{4}$$

The carbon balance is calculated as follows:

$$\text{Carbon balance} = \frac{F_{CO2,out} + F_{CH4,out} + F_{CO,out}}{F_{CO2,in}} \times 100\% \tag{5}$$

where $F_{i,\,in}$ stands for the inlet flow rate of gas i and $F_{i,\,out}$ stands for the outlet flow rate of gas i. During the reaction, the carbon balance results were always higher than 99.5 %.

The reaction order measurements were conducted at 350 °C with the conversion kept at 10 %. The gas mixture contained 15-25 mL/min CO_2, 70-90 mL/min H_2 in Ar balance, at a total flow rate of 200 mL/min.

The turnover frequency (TOF) is determined on the basis of exposed Ni, which is calculated from the result of H_2-chemisorption.

$$\mathrm{TOF} = \frac{CO_2\ consumption\ rate}{amount\ of\ Ni\ exposed} \tag{6}$$

3. RESULTS AND DISCUSSION

3.1 Catalyst Structure

The series of 15NiSi catalysts with different Mg loading were characterized via N_2 isothermal sorption experiments to determine the BET surface area. As illustrated in Table 1, no significant difference in BET area was discovered with increasing Mg loading.

To evaluate the reduction degree of the different catalysts, H_2-TPR was conducted (Figure S1(a)). As MgO and SiO_2 are not reducible in the considered temperature range, all the peaks detected were ascribed to the reduction of NiO. The main reduction peak slightly shifted to higher temperature upon MgO addition. For all catalysts, NiO could be completely converted into metallic Ni below 600 °C. No further reduction was detected, even when the temperature was raised to 900 °C. Therefore, 600 °C was selected as pretreatment condition for the catalysts before the activity experiments.

After reduction in H_2/Ar at 600 °C for 30 min, the samples were characterized by XRD in order to detect the crystallite phase and size. As indicated in Figure S1(b), only characteristic peaks corresponding to metallic Ni could be detected (PDF: 00-004-0850) with no trace of MgO or Mg diffractions. The Scherrer equation was used to calculate the Ni crystallite size, which decreased with increasing Mg loading (Table 1), an observation in line with others[51, 52].

Table 1. Physicochemical properties of the MgO/Ni/SiO_2 catalysts

sample	BET surface area (m^2/g)	Metallic surface area (x 10^{-6} mol Ni/g)[a]	Ni crystallite size (nm)[b]	Ni particle size (nm)[c]
0Mg15NiSi	153.5	12.0	32	35
0.5Mg15NiSi	153.6	8.9	30	-
1Mg15NiSi	160.1	6.9	29	24
1.5Mg15NiSi	159.6	6.4	28	-
3Mg15NiSi	150.2	5.9	21	21

[a] Determined by H_2-chemisorption

[b] Calculated from XRD patterns

[c] Determined by TEM

TEM was carried out to determine the particle size distribution for reduced catalysts without and with Mg (Figure S2). In both, the metallic Ni particles vary in size from 5 to 60 nm. However, in analogy with XRD (Table 1), the average particle size is smaller for 3Mg15NiSi (21 nm) and 1Mg15NiSi (24 nm) than on 0Mg15NiSi (35 nm). The latter can result from the interaction between MgO and NiO[22, 51].

HAADF-STEM with EDX-mapping was conducted on 1.5Mg15NiSi to locate Mg (Figure 1). MgO was found distributed not only on SiO_2, but also on metallic Ni. From the overlay of the Ni and Mg elemental maps (Figure 1(f)), MgO seems to surround the Ni particles as a shell. The sample with 3 wt.% Mg loading exhibits an analogous element distribution (Figure S3).

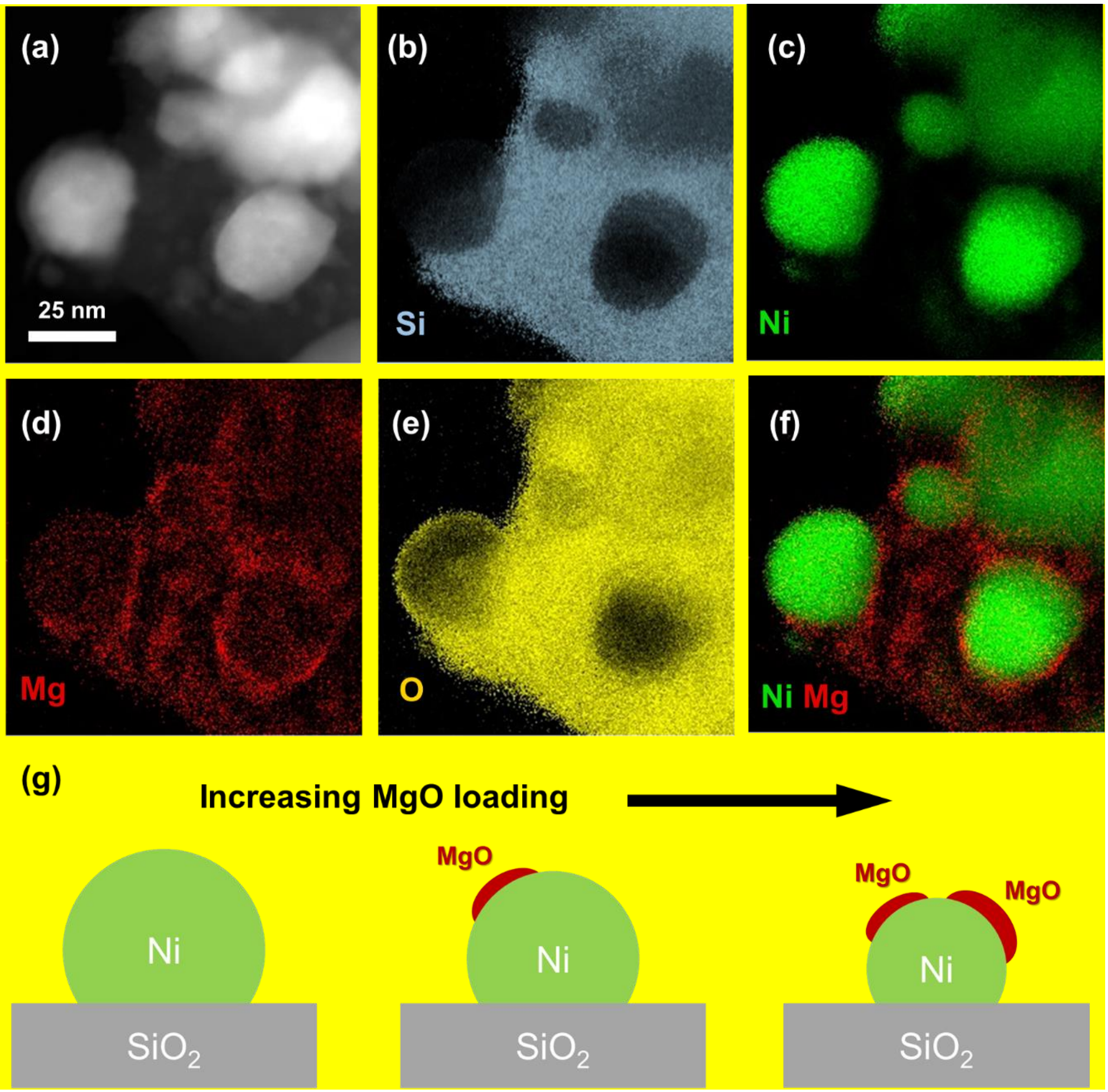

Figure 1. (a) HAADF-STEM and (b-f) EDX elemental mapping of reduced 1.5Mg15NiSi. (g) Catalyst models of NiSi and MgNiSi with increasing MgO loading, leading to smaller Ni particle size.

To further verify the structure, H_2-chemisorption was applied to determine the amount of exposed Ni. The metallic surface area decreased with increasing Mg loading, almost by half upon going from 0 to 3MgO (Table 1). Although the addition of MgO leads to smaller Ni crystallites as indicated by XRD and TEM, it does, in contrast, not lead to higher exposed metallic surfaces. Hence, it is concluded that MgO reduces the exposed surface of the Ni particles. Based on these characterization results, a catalyst model can be proposed, where MgO is dispersed on the surface of metallic Ni (Figure 1(g)).

In situ Ni K edge QXAS was carried out to detail the local electronic and structural properties of Ni in as-prepared and reduced 0Mg15NiSi and 3Mg15NiSi as representative catalysts (Figure S4(a and b)). For as-prepared samples, the Ni state corresponds to NiO. After reduction, the XAS spectrum bears strong resemblance with Ni foil, suggesting that NiO is fully reduced, even in the presence of MgO. EXAFS modelling of the aforementioned spectra (Figure S5, fitting parameters in Table S1 and Table S2) further identifies NiO in the initial state, while at the end of TPR, only contributions related to metallic Ni are resolved.

Following H_2-TPR, CO_2 methanation was carried out, with simultaneous collection of Ni K edge spectra. As shown in Figure S4, no significant difference in white line appears between Ni foil, the sample after reduction and after methanation. This indicates no oxidation by CO_2 occurs during the methanation reaction and Ni remains in metallic state for the catalysts with and without MgO. It must be noted that the differences in FT-EXAFS intensities between the states after reduction and after methanation (Figure S4C-D) are a temperature effect[41]. Since the reduced sample and sample after methanation were measured at 600 °C and 350 °C, respectively, this results in a higher Debye-Waller effect in the former case, yielding lower intensities within the corresponding FT-

EXAFS results. The fitting result (Figure S6 and Table S3) further proves no Ni-O bonds are detected after *in situ* methanation.

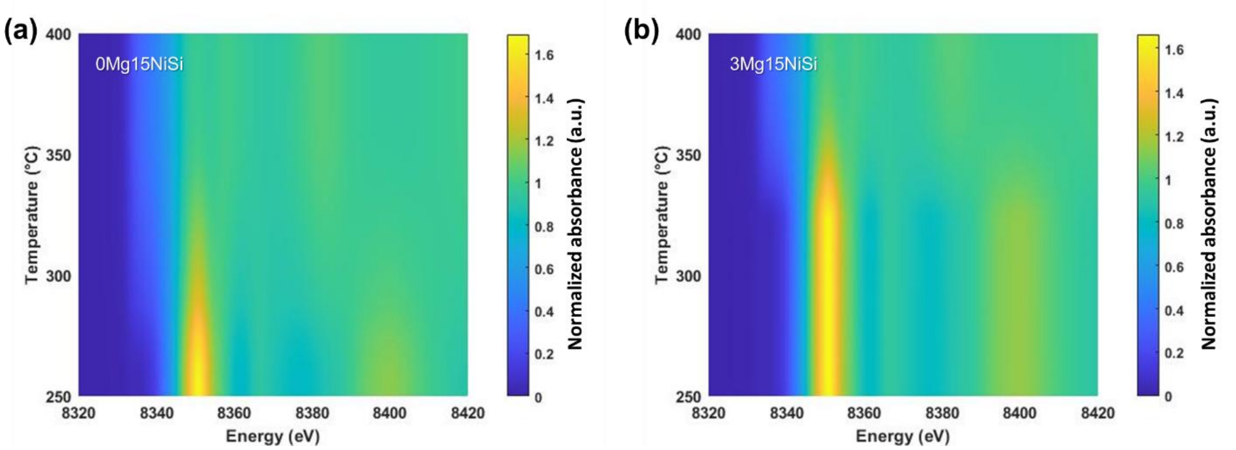

Figure 2. *In situ* QXANES spectra as a function of time/temperature during H_2-TPR of (a) 0Mg15NiSi and (b) 3Mg15NiSi at the Ni K edge. Color bar: legend for normalized absorbance.

Although the final state of samples with and without MgO are the same, MgO does have a considerable influence upon the Ni reduction. Figure 2 shows 2D intensity plots of the XANES region of the spectra at the Ni K edge for both catalysts during H_2-TPR. With increasing temperature, reduction of NiO takes place, occurring at higher reduction temperature for 3Mg15NiSi than for 0Mg15NiSi, ~350 vs. ~300 °C. MCR-ALS analysis for the catalysts under H_2-TPR (Figure S7) and EXAFS analysis (Figure S8) extracts two components from the *in situ* QXAS data. EXAFS fitting of these components shows they correspond to NiO (Component 1) and metallic Ni (Component 2). The contribution of the two components as a function of time (temperature) is displayed in Figure S7. 100 % of NiO is reduced into metallic Ni for both catalysts.

From the first derivative of the MCR-ALS profiles (Figure S8(c and f)), the reduction of 0Mg15NiSi sets in at 252 °C and ends at 368 °C, while for 3Mg15NiSi it starts at 320 °C and is finished at 422 °C. This agrees well with the reduction peaks in conventional TPR, shifting to higher temperature when MgO is present (Figure S1(a)) and the evolution of the whiteline in *in situ* XANES (Figures 2(a and b)). According to literature, NiO can interact strongly with MgO, forming mixed oxide phases, which can induce a delay in the reduction of NiO[32, 34, 53, 54]. The upward shift of the reduction temperature indicates there is indeed interaction between NiO and MgO, which leads to delayed reduction of NiO in 3Mg15NiSi compared to 0Mg15NiSi.

3.2 Catalytic Performance in CO_2 Methanation

Catalytic performance tests for CO_2 methanation were executed at 350 °C under 1.2 bar. Only CO and CH_4 were detected as products. Figure 3(a) shows a notable increase of the production rate of CH_4 and a decrease of CO production for 1Mg15NiSi compared to 0Mg15NiSi. 1Mg0NiSi, used as a control experiment, shows a negligible level of conversion. The influence of MgO loading on CH_4 selectivity was further tested on a series of xMg15NiSi with varying Mg loading, which shows MgO addition helps to increase the CH_4 selectivity, but lowers the CO_2 conversion. Nevertheless, the production rate of the desired product CH_4 was enhanced with only 0.5wt.% MgO, reaching a maximum when the loading is 1wt.% (Figure S9(a)). A further increase in Mg loading continues to increase the CH_4 selectivity, while reducing the productivity. The intrinsic activity of the catalysts is reflected by their TOF. As shown in Figure S9(b), MgO addition has little impact on the TOF of CO_2, while slightly increasing the TOF of CH_4 and decreasing the one of CO. The decreased CO_2 conversion with MgO addition (Figure S9(a)) is caused by the coverage of Ni by MgO, which reduces the number of exposed Ni sites. The trend of the CH_4 TOF indicates the intrinsic activity of Ni is strongly influenced by MgO up to a loading of 1.5% (Figure S9(b)). Moreover, both catalysts present good stability in a 300 min test (Figure S9(c)), an important requirement for Ni-based catalysts used in CO_2 methanation[21, 55, 56].

Previous work has proven that CH_4 selectivity is CO_2 conversion-dependent[24, 57]. For both Ni catalysts, 0Mg15NiSi and 1Mg0NiSi, the CH_4 selectivity rises with CO_2 conversion (Figure 3(b)). Comparing both catalysts at the same conversion, however, shows much higher selectivity for the MgO-modified sample.

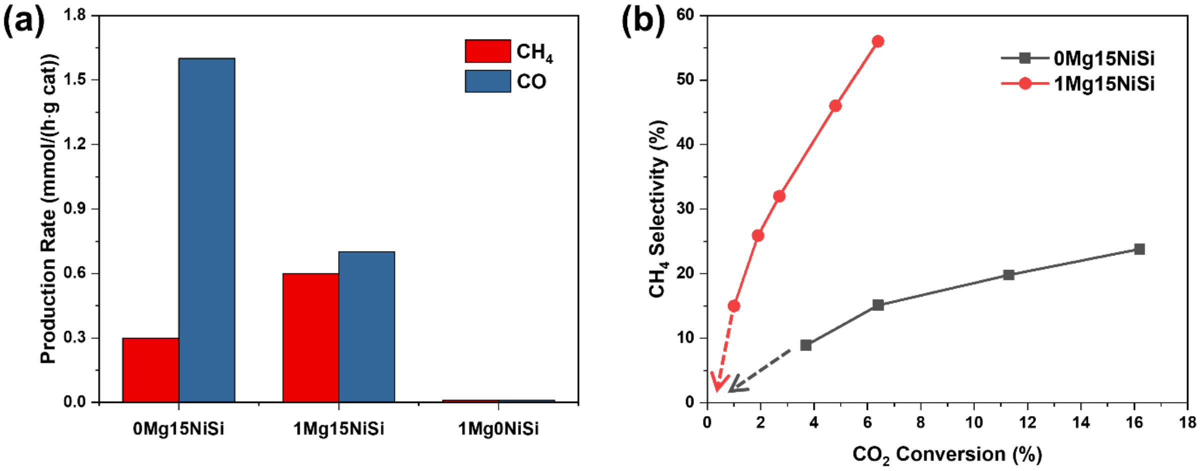

Figure 3. (a) Rate of CH_4 and CO production over 0Mg15NiSi, 1Mg15NiSi and 1Mg0NiSi under the same reaction conditions. Total flow rate: 200 mL/min; CO_2:H_2:Ar = 1:4:5, 350 °C; 0.1 g catalyst. (b) CH_4 selectivity versus CO_2 conversion plot for 0Mg15NiSi and 1Mg15NiSi. CO_2:H_2:Ar = 1:4:5, 350 °C; Conversion was adjusted by changing space velocity.

To verify a possible particle size effect, a series of NiSi samples with different Ni loadings were synthesized and tested. The particle size of Ni (Figure S10(a)) decreases with decreasing Ni loading. For 0.5NiSi, no Ni diffractions are discerned, meaning that either the Ni loading is too low for detection, or the crystallite size is below 3nm or Ni is amorphous. Still, the variation of CH_4 selectivity at the same CO_2 conversion, induced by these different particle sizes, is quite small (~5%) (Figure S10(b)). Therefore, the pronounced improvement of CH_4 selectivity for the MgO-added samples is considered associated with the interaction between MgO and Ni, rather than with the Ni particle size.

XRD and TEM measurements imply that MgO decreases the average particle size of Ni, which doesn't exclude the presence of smaller sized Ni particles or NiMgO solid solution. To verify the latter presence, the position of the main NiO(200) diffraction in as prepared catalysts was considered (Figure S10 (c-d)). With increasing MgO loading, the NiO diffraction was found to shift slightly towards lower angle, where an MgO diffraction is situated, indicative of NiMgO solid solution being formed at the NiO-MgO interface[9, 24, 58], The latter can also be deduced from the EDX elemental mapping of reduced 1.5Mg15NiSi in Figure 1(f), showing mixed Ni-Mg regions surrounding the Ni particles. The reduction process can further lead to segregation of nanosized Ni from the NiMgO solid solution and this 'Ni leaching' process, induced by the strong interaction between NiO and MgO, is held responsible for the smaller Ni particle size upon MgO addition[32, 41].

However, the variation of CH_4 selectivity at the same CO_2 conversion, induced by a difference in particle size from <3 to 32 nm, is quite small (5%) (Figure S10(b)). Therefore, the pronounced improvement of CH_4 selectivity for the MgO-added samples is considered associated with the interaction between MgO and Ni, rather than with Ni particle size.

3.3 Reaction pathway identification

As indicated in Scheme 1, CO_2 methanation might proceed through two pathways: indirect and direct. In the indirect pathway, CH_4 is produced by the hydrogenation of CO, which is also the byproduct produced through RWGS reaction. On the contrary, CH_4 is formed without going through the intermediate CO*.

Since CO is the main byproduct when using NiSi as catalyst, there is no doubt that a considerable amount of CO_2 is converted to CO* through RWGS, which constitutes the initial part of the indirect methanation pathway. However, as displayed in Figure 3(b), the CH_4 selectivity approaches zero, when the CO_2 conversion is extrapolated to zero. The latter is a representative feature of sequential reactions, indicating that CH_4 is a consecutive product produced from CO[24, 59, 60].

In situ DRIFTS experiments were performed to monitor the reaction intermediates and thereby identify the reaction pathway. During methanation, bands for the formyl group (HCO*), located at 1743 cm^{-1} and some carbonates (1550-1510 cm^{-1}) are detected on both catalysts. HCO* appears as reaction intermediate in both the direct and one indirect pathway (Scheme 1). The carbonate species on the other hand, formed upon adsorption of CO_2, are only active in the direct pathway[7]. However, as it has been proved that the reaction follows an indirect pathway, carbonate species mostly act as spectators. A recent study regarding a Ni catalyst confirms that carbonate does not participate in the reaction[61]. Infrared features for adsorbed CO* (located between 2000 – 1900 cm^{-1}) are not observed in DRIFTS during the reaction. Probably, they readily desorb, forming CO(g), or further hydrogenate into HCO*, causing the concentration of CO* to remain under a detectable coverage. Similarly, no C-H band was observed during methanation, e.g. at 3003 cm^{-1} representing the stretching vibration of CH_4. This can be related to the very low selectivity to CH_4, caused by the low conversion under DRIFTS conditions. Overall, the DRIFTS spectra of the catalysts with and without MgO are quite similar, which indicates MgO addition does not actually change the reaction pathway, but instead changes the rate of certain steps in a specific pathway.

A transient DRIFTS test was also performed, while removing CO_2 from the feed, leaving only H_2. After switching off the CO_2 stream, a C-H band started to appear around 3003 cm^{-1}, while the

HCO* and carbonate bands disappeared. This result of transient DRIFTS indicates that HCO* is actively being removed by reaction with H_2 producing CH_4, hence HCO* is no spectator species.

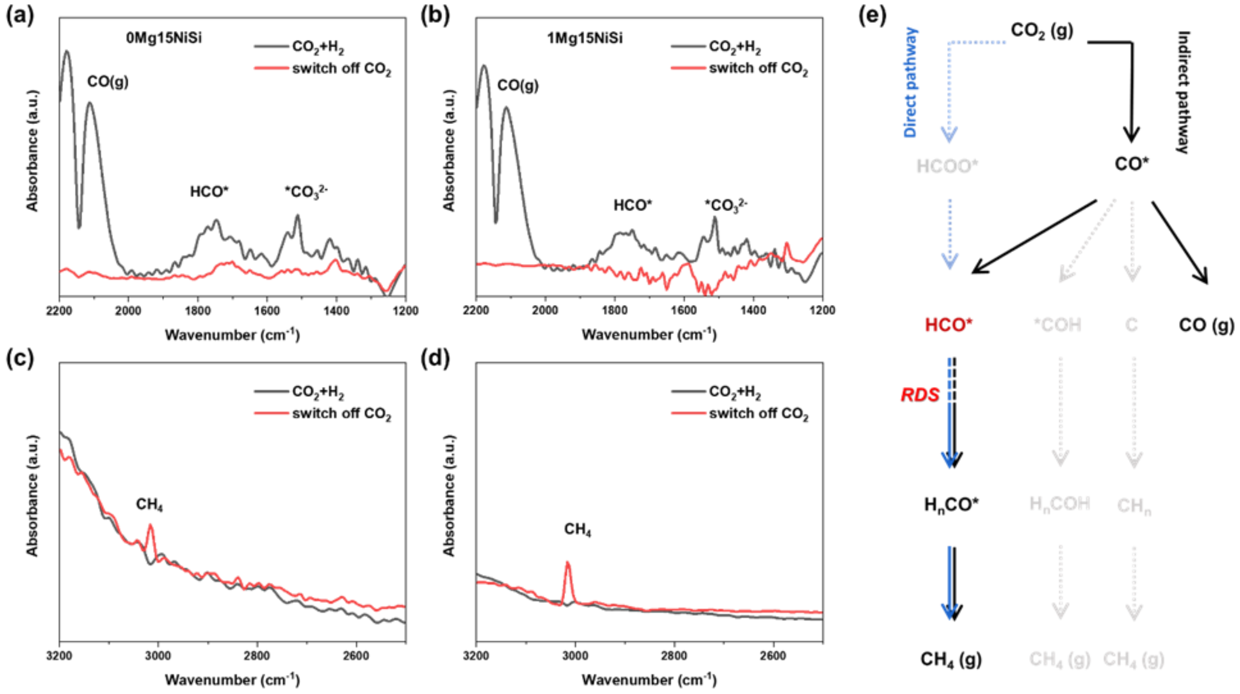

Figure 4. *In situ* DRIFTS spectra of 0Mg15NiSi (a) (c) and 1Mg15NiSi (b) (d) at 350 °C, under CO_2+H_2 and after removing CO_2 from the feed. 1743 cm^{-1}: formyl group. 1550-1510 cm^{-1}: carbonate species. (e) Proposed reaction pathway for NiSi and MgNiSi. Light dash lines: less probable pathways. Solid lines: confirmed pathways.

As indicated in Scheme 1, the indirect pathway consist of three different directions with different representative intermediate: C, *COH and HCO*. The transformation from HCO* to CH_4 has been validated by *in situ* and transient DRIFTS. In addition, we tend to believe the reaction routes going through *COH to CH_4 are less probable as the associated intermediates are not observed.

Still, carbon hydrogenation cannot be excluded, because carbon is not detectable by DRIFTS. In order to examine the likelihood of the carbon hydrogenation pathway, a series of temperature programmed reactions were conducted. The pathway from CO to CH_4 going through carbon can be divided into two steps, CO dissociation and carbon hydrogenation (Scheme 1). Thus, the overall surface reaction CO+H_2 TPRS as well as the two steps TP-CO dissociation and C-TPH are tested separately (Figure S12). The CO dissociation reaction is so fast that CO_2 and C start to form as soon as CO is introduced at 50 °C (Figure S12(b)). Then again, the carbon hydrogenation reaction is faster over 0Mg15NiSi (Figure S12(c), which is in contrast with the fact that 1Mg15NiSi is more active for CO methanation (Figure S12(a)). Thus, methanation over MgO promoted Ni is unlikely to follow the carbon hydrogenation pathway. Therefore, the methanation reaction is believed to proceed from CO_2 over HCO* to CH_4 on Ni/SiO_2 and MgO/Ni/SiO_2 (Figure 4(e)).

3.4 Effect of MgO addition on the reaction pathway

The kinetic experiments were performed to reveal the nature of methanation on Ni/SiO_2 as well as understanding the effect of MgO. Before starting the actual tests, the absence of external and internal mass transfer limitations was verified using the Carberry number and Weisz-Prater criterion. Table 2 shows the dependence of the CH_4 and CO formation rate on the partial pressure of CO_2 and H_2, determined at 350 °C (fittings displayed in Figure S11).

For the RWGS reaction, which produces CO, the reaction orders with respect to CO_2 partial pressure are negative, varying between -0.45 ~ -0.22. These negative values suggest a high coverage of CO_2-derived intermediates, which is likely to inhibit the formation of CO. The reaction orders of H_2 are ~0 for CO formation, suggesting either adsorbed hydrogen is not involved in the rate determining step (RDS) of RWGS, or the coverage of H* is abundant enough for CO formation, and hence not a limiting factor for CO formation.

For the methanation process, the reaction orders with respect to CO_2 partial pressure are about -0.9. The negative number again shows the coverage with CO_2-derived intermediates is so high that it inhibits reaction. In addition, the reaction orders of H_2 for CH_4 formation are positive, pointing to a relatively low coverage of adsorbed hydrogen. As a result, increasing the partial pressure of H_2 has a promotional effect on CH_4 formation. Based on the negative values of reaction order of CO_2, it is suggested that CO_2-derived intermediates strongly adsorb on the catalyst surface, thereby blocking free sites for H_2 adsorption, which inhibits the formation of CH_4.

Based on the results of reaction order, it is rational to postulate that the removal of CO_2-derived intermediates with the help of H_2 constitutes the RDS. *In situ* and transient DRIFTS study has proved that HCO* intermediate accumulated on the surface during the reaction. Removal of CO_2 from the reactants lead to a consumption of HCO*, accompanied by the increase of CH_4. Thus, it is proposed that HCO* as intermediate is so stable that the high surface coverage of HCO* blocks free sites and prevents the dissociation of H_2, which impedes the subsequent hydrogenation to produce CH_4. When CO_2 is removed from the feed (Figure 4(a-d)), HCO* is gradually consumed, freeing sites for H_2 dissociation. As a consequence, the RDS is the HCO* hydrogenation (Figure 4(e)).

Table 2. Reaction order for CH_4 and CO formation over 0Mg15NiSi, 1Mg15NiSi and 3Mg15NiSi.

	Order for CH_4 formation	Order for CO formation

	CO_2	H_2	CO_2	H_2
0Mg15NiSi	-0.93	0.50	-0.45	-0.04
1Mg15NiSi	-0.89	0.44	-0.28	-0.06
3Mg15NiSi	-0.73	0.11	-0.05	0.11

In addition, the reaction order give us some insight into the effect of MgO for CH_4 formation. As the MgO loading increases from 0 to 3wt.%, the reaction order respect to CO_2 increase from -0.93 to -0.73. At the same time, the reaction order for H_2 for CH_4 formation decreases from 0.50 to 0.11. The increased negative value of CO_2 reaction order implies a lower coverage of CO_2-derived intermediate, probably to be HCO*, which results in a mitigated poisoning effect after MgO addition. The lower value of reaction order of H_2 implies a higher hydrogen coverage is present on MgO promoted catalysts[62] as a consequence of decrease HCO* coverage.

To further investigate the role of MgO addition, CO_2+H_2 TPSR experiments were conducted over 0Mg15NiSi and 1Mg15NiSi. As indicated in Figure 5(a) and (b), the onset temperature of CO evolution lies at 150 °C for both catalysts, which indicates CO_2 starts to be activated around 150 °C through RWGS. In contrast, the CH_4 onset temperature is 172 °C over 0Mg15NiSi and 150 °C over 1Mg15NiSi. Thus, the higher onset temperature of CH_4 implies that the production of CH_4 on 0Mg15NiSi has to overcome a higher energy barrier than over 1Mg15NiSi. Apparent activation energies were also calculated based on the results of the CO_2+H_2 TPSR (Table S4). In line with the onset temperature, the activation energies of CO formation are similar for both catalysts, which indicates the same reaction mechanism applies over catalysts with and without MgO (~80 kJ/mol). However, the activation energy for CH_4 formation over 0Mg15NiSi is with 90.0 kJ/mol considerably higher than that over 1Mg15NiSi (76.3 kJ/mol). The change in apparent activation energy may refer to a change in pathway and/or energy barrier. However, in this specific case, the reaction pathway is not affected by the addition of MgO, remaining the same as unmodified Ni/SiO_2. As the energy barrier is closely related to the RDS, which is identified as HCO* hydrogenation, it is rational to conclude that the addition of MgO helps to reduce the energy barrier of HCO* hydrogenation.

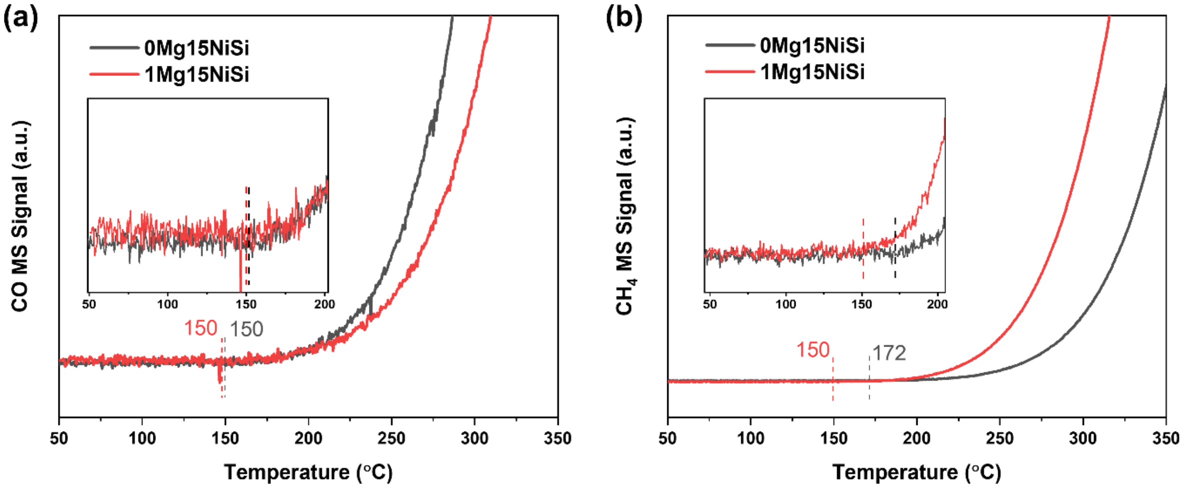

Figure 5. CO_2+H_2 TPSR profiles of 0Mg15NiSi and 1Mg15NiSi. (a) CO MS signal and (b) CH_4 MS signal. Conditions were 0.1 g catalyst, CO_2: H_2: Ar= 1: 4: 5, total flow rate = 200 mL/min, i.e. exactly the same as for the reactivity test, ensuring a conversion below 10%.

Based on the characterization in Figure 1 and Table 1, the addition of MgO leads to the formation of an explicit metal oxide-metal interface and its extent can easily be tuned by means of the MgO loading. The chemical property changes induced by the MgO/Ni interface were investigated through *in situ* QXAS during CO_2 oxidation of a reduced sample (Figure 6). On 3Mg15NiSi, a partial oxidation of metallic Ni was observed, while nothing changed for 0Mg15NiSi.

A similar phenomenon was observed in an investigation of Ni supported on $MgAl_2O_4$[63], where the creation of an interface entailed metal-support interaction, which strongly influenced the oxidation of Ni by CO_2. The effect of the Ni/$MgAl_2O_4$ interface not only depended on the Ni particle size, i.e. the interface extent, but it also provided a diffusion channel for particle oxidation. In the present work, the result of *in situ* QXAS implies that the construction of a MgO/Ni interface induces a similar interaction, now between Ni metal and MgO as oxide promoter. The latter provides new sites with high activity and decreases the energy barrier of methanation, which makes it chemically different from unpromoted Ni.

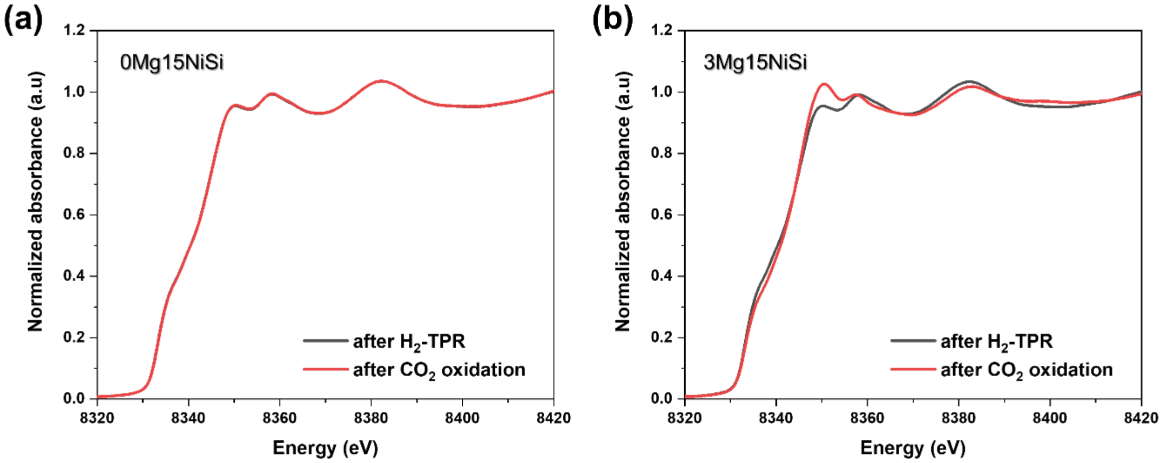

Figure 6. *In situ* QXANES spectra for (a) 0Mg15NiSi and (b) 1Mg15NiSi after H_2-TPR and after CO_2 oxidation at 600°C.

Based on the above results, a possible reaction scheme for CO_2 methanation is proposed (Scheme 2). Without MgO, the energy barrier for the RDS, the hydrogenation process of HCO* on the Ni surface, is high, thus the formation rate of CH_4 is slow. In addition, stable HCO* species cover the

Ni surface, which prevents H_2 dissociation. The resulting low coverage of hydrogen only suffices for CO_2 hydrogenation forming CO, but remains insufficient for CH_4 formation, which requires 4 molecular H_2.

After MgO addition, a MgO/Ni interface forms which has specific chemical properties, different from a regular Ni surface. The associated metal oxide-metal interaction will likely involve a charge transfer, as shown by the shift in reduction temperature (Figure 2), and the creation of new active sites[37, 64, 65]. As indicated in Figure 6b, the energy barrier of RDS is lower for MgO-modified Ni catalysts, promoting CH_4 formation. The faster consumption of HCO* leaves more sites for H_2 adsorption and dissociation and hence higher H_2 coverage, as evidenced by the reaction order. The latter also contributes to an enhanced formation of CH_4.

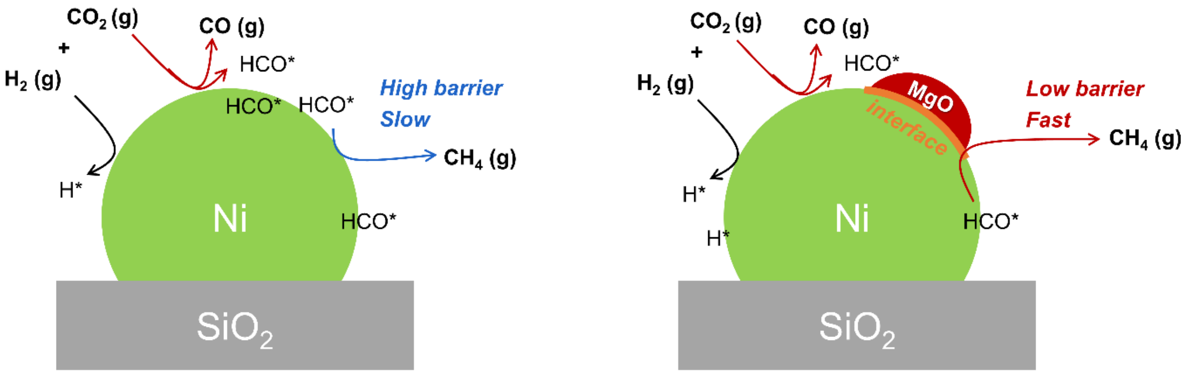

Scheme 2. Proposed reaction mechanism for CO_2 methanation over Ni/SiO_2 and $MgO/Ni/SiO_2$ catalysts.

4. CONCLUSION

Through tuning of metal oxide-metal interaction by means of MgO decoration, the catalytic performance of Ni/SiO_2 in CO_2 methanation has a considerable enhancement. The performance of the modified catalysts was benchmarked against a non-promoted catalyst investigated under the same reaction conditions.

A mechanistic understanding of the enhanced CH_4 selectivity in CO_2 methanation over MgO-promoted Ni/SiO_2 catalysts has been acquired. Based on combined high-resolution STEM-EDX, *in situ* QXAS and a series of temperature programmed experiments, a catalyst model is built, where MgO partially covers the surface of metallic Ni. The so formed MgO/Ni interface exhibits metal oxide-metal interaction. Through a kinetic study and in situ DRIFTS, HCO* is found to be the key intermediate, hindering the subsequent hydrogenation process, hence hydrogenation of HCO* is determined as the RDS. The formation of the MgO/Ni interface however helps to decrease the RDS energy barrier, which will enhance the conversion of the reaction intermediate HCO*, resulting in a higher CH_4 selectivity. As such, this work illustrates the key correlation between the metal oxide-metal interface and CH_4 selectivity, which serves as example on the importance of the interplay between Ni metal and MgO.

CRediT author statement

Yufei Xie: Conceptualization, Methodology, Investigation, Formal analysis, Writing – original draft, Writing – review & editing. **Valentijn De Coster:** Software, Data Curation, Writing – original draft. **Lukas Buelens:** Investigation. **Hilde Poelman:** Writing – review & editing, Supervision, Funding acquisition. **Bensu Tunca:** Investigation. **Jin-Won Seo:** Investigation. **Christophe Detavernier:** Supervision, Funding acquisition. **Vladimir Galvita:** Conceptualization, Writing – review & editing, Supervision, Funding acquisition.

Declaration of Competing Interest

The authors declare that there are no conflicts of interest.

Acknowledgements

This work is part of a project funded by the Fund for Scientific Research Flanders (project number G032920N). V.D.C. acknowledges a personal grant from the Research Fund of Ghent University (BOF; 01D00719). The authors acknowledge the assistance from the ROCK staff for a smooth beamtime (SOLEIL, proposal 20210504). This work was supported by a public grant overseen by the French National Research Agency (ANR) as part of the “Investissements d’Avenir” program (reference: ANR-10-EQPX-45). The authors acknowledge Dr. S.P. Sree from Structural Materials (SCALINT), KU Leuven, for the STEM-EDX images.

Appendix A. Supporting information

Supplementary data associated with this article can be found in the online version.

REFERENCES

[1] X. Su, J. Xu, B. Liang, H. Duan, B. Hou, Y. Huang, Catalytic Carbon Dioxide Hydrogenation to Methane: A Review of Recent Studies, J. Energy Chem. 25 (2016) 553-565. https://doi.org/10.1016/j.jechem.2016.03.009.
[2] W. Wang, S. Wang, X. Ma, J. Gong, Recent Advances in Catalytic Hydrogenation of Carbon Dioxide, Chem. Soc. Rev. 40 (2011) 3703-3727. https://doi.org/10.1039/c1cs15008a.
[3] M. Younas, L. Loong Kong, M.J.K. Bashir, H. Nadeem, A. Shehzad, S. Sethupathi, Recent Advancements, Fundamental Challenges, and Opportunities in Catalytic Methanation of CO_2, Energy Fuels 30 (2016) 8815-8831. https://doi.org/10.1021/acs.energyfuels.6b01723.
[4] Y. Wang, L.R. Winter, J.G. Chen, B. Yan, CO_2 Hydrogenation over Heterogeneous Catalysts at Atmospheric Pressure: from Electronic Properties to Product Selectivity, Green Chem. 23 (2021) 249-267. https://doi.org/10.1039/d0gc03506h.
[5] T. Schaaf, J. Grünig, M.R. Schuster, T. Rothenfluh, A. Orth, Methanation of CO_2 - storage of Renewable Energy in a Gas Distribution System, Energy Sustain. Soc. 4 (2014) 2. https://doi.org/10.1186/s13705-014-0029-1.
[6] C. Heine, B.A. Lechner, H. Bluhm, M. Salmeron, Recycling of CO_2: Probing the Chemical State of the Ni(111) Surface during the Methanation Reaction with Ambient-Pressure X-Ray Photoelectron Spectroscopy, J. Am. Chem. Soc. 138 (2016) 13246-13252. https://doi.org/10.1021/jacs.6b06939.
[7] C. Vogt, E. Groeneveld, G. Kamsma, M. Nachtegaal, L. Lu, C.J. Kiely, P.H. Berben, F. Meirer, B.M. Weckhuysen, Unravelling Structure Sensitivity in CO_2 Hydrogenation over Nickel, Nat. Catal. 1 (2018) 127-134. https://doi.org/10.1038/s41929-017-0016-y.
[8] X. Jia, X. Zhang, N. Rui, X. Hu, C.-j. Liu, Structural effect of Ni/ZrO_2 catalyst on CO_2 methanation with enhanced activity, Appl. Catal. B 244 (2019) 159-169. https://doi.org/10.1016/j.apcatb.2018.11.024.
[9] Z. Hao, J. Shen, S. Lin, X. Han, X. Chang, J. Liu, M. Li, X. Ma, Decoupling the Effect of Ni Particle Size and Surface Oxygen Deficiencies in CO_2 Methanation over Ceria Supported Ni, Appl. Catal. B 286 (2021) 119922-119932. https://doi.org/10.1016/j.apcatb.2021.119922.
[10] J.H. Kwak, L. Kovarik, J. Szanyi, CO_2 Reduction on Supported Ru/Al_2O_3 Catalysts: Cluster Size Dependence of Product Selectivity, ACS Catal. 3 (2013) 2449-2455. https://doi.org/10.1021/cs400381f.
[11] S. Chen, A.M. Abdel-Mageed, M. Dyballa, M. Parlinska-Wojtan, J. Bansmann, S. Pollastri, L. Olivi, G. Aquilanti, R.J. Behm, Raising the CO_x Methanation Activity of a Ru/gamma-Al_2O_3 Catalyst by Activated Modification of Metal-Support Interactions, Angew. Chem. Int. 59 (2020) 22763-22770. https://doi.org/10.1002/anie.202007228.

[12] J.C. Matsubu, S. Zhang, L. DeRita, N.S. Marinkovic, J.G. Chen, G.W. Graham, X. Pan, P. Christopher, Adsorbate-Mediated Strong Metal-Support Interactions in Oxide-Supported Rh Catalysts, Nat. Chem. 9 (2017) 120-127. https://doi.org/10.1038/nchem.2607.
[13] J.C. Matsubu, V.N. Yang, P. Christopher, Isolated Metal Active Site Concentration and Stability Control Catalytic CO_2 Reduction Selectivity, J. Am. Chem. Soc. 137 (2015) 3076-3084. https://doi.org/10.1021/ja5128133.
[14] J.H. Kwak, L. Kovarik, J. Szanyi, Heterogeneous Catalysis on Atomically Dispersed Supported Metals: CO_2 Reduction on Multifunctional Pd Catalysts, ACS Catal. 3 (2013) 2094-2100. https://doi.org/10.1021/cs4001392.
[15] X. Wang, H. Shi, J.H. Kwak, J. Szanyi, Mechanism of CO_2 Hydrogenation on Pd/Al_2O_3 Catalysts: Kinetics and Transient DRIFTS-MS Studies, ACS Catal. 5 (2015) 6337-6349. https://doi.org/10.1021/acscatal.5b01464.
[16] W. Chen, R. Pestman, B. Zijlstra, I.A.W. Filot, E.J.M. Hensen, Mechanism of Cobalt-Catalyzed CO Hydrogenation: 1. Methanation, ACS Catal. 7 (2017) 8050-8060. https://doi.org/10.1021/acscatal.7b02757.
[17] C. Yang, S. Liu, Y. Wang, J. Song, G. Wang, S. Wang, Z.J. Zhao, R. Mu, J. Gong, The Interplay between Structure and Product Selectivity of CO_2 Hydrogenation, Angew. Chem. Int. 58 (2019) 11242-11247. https://doi.org/10.1002/anie.201904649.
[18] Z. Zhang, C. Shen, K. Sun, X. Jia, J. Ye, C.-j. Liu, Advances in Studies of the Structural Effects of Supported Ni Catalysts for CO_2 Hydrogenation: from Nanoparticle to Single Atom Catalyst, J. Mater. Chem. A 10 (2022) 5792-5812. https://doi.org/10.1039/d1ta09914k.
[19] L. Shen, J. Xu, M. Zhu, Y.-F. Han, Essential Role of the Support for Nickel-Based CO_2 Methanation Catalysts, ACS Catal. 10 (2020) 14581-14591. https://doi.org/10.1021/acscatal.0c03471.
[20] S. Kattel, W. Yu, X. Yang, B. Yan, Y. Huang, W. Wan, P. Liu, J.G. Chen, CO_2 Hydrogenation over Oxide-Supported PtCo Catalysts: The Role of the Oxide Support in Determining the Product Selectivity, Angew. Chem. Int. 55 (2016) 7968-7973. https://doi.org/10.1002/anie.201601661.
[21] B. Mutz, M. Belimov, W. Wang, P. Sprenger, M.-A. Serrer, D. Wang, P. Pfeifer, W. Kleist, J.-D. Grunwaldt, Potential of an Alumina-Supported Ni3Fe Catalyst in the Methanation of CO_2: Impact of Alloy Formation on Activity and Stability, ACS Catal. 7 (2017) 6802-6814. https://doi.org/10.1021/acscatal.7b01896.
[22] M. Guo, G. Lu, The Effect of Impregnation Strategy on Structural Characters and CO_2 Methanation Properties over MgO Modified Ni/SiO_2 Catalysts, Catal. Commun. 54 (2014) 55-60. https://doi.org/10.1016/j.catcom.2014.05.022.
[23] M.-C. Silaghi, A. Comas-Vives, C. Copéret, CO_2 Activation on Ni/γ–Al_2O_3 Catalysts by First-Principles Calculations: From Ideal Surfaces to Supported Nanoparticles, ACS Catal. 6 (2016) 4501-4505. https://doi.org/10.1021/acscatal.6b00822.
[24] C.-S. Chen, C.S. Budi, H.-C. Wu, D. Saikia, H.-M. Kao, Size-Tunable Ni Nanoparticles Supported on Surface-Modified, Cage-Type Mesoporous Silica as Highly Active Catalysts for CO_2 Hydrogenation, ACS Catal. 7 (2017) 8367-8381. https://doi.org/10.1021/acscatal.7b02310.
[25] Y. Guo, S. Mei, K. Yuan, D.-J. Wang, H.-C. Liu, C.-H. Yan, Y.-W. Zhang, Low-Temperature CO_2 Methanation over CeO_2-Supported Ru Single Atoms, Nanoclusters, and Nanoparticles Competitively Tuned by Strong Metal–Support Interactions and H-Spillover Effect, ACS Catal. 8 (2018) 6203-6215. https://doi.org/10.1021/acscatal.7b04469.

[26] S. Li, Y. Xu, Y. Chen, W. Li, L. Lin, M. Li, Y. Deng, X. Wang, B. Ge, C. Yang, S. Yao, J. Xie, Y. Li, X. Liu, D. Ma, Tuning the Selectivity of Catalytic Carbon Dioxide Hydrogenation over Iridium/Cerium Oxide Catalysts with a Strong Metal-Support Interaction, Angew. Chem. Int. 56 (2017) 10761-10765. https://doi.org/10.1002/anie.201705002.
[27] L. Chen, L. Kovarik, D. Meira, J. Szanyi, Differentiating and Understanding the Effects of Bulk and Surface Mo Doping on CO_2 Hydrogenation over Pd/Anatase-TiO_2, ACS Catal. 12 (2022) 13492-13500. https://doi.org/10.1021/acscatal.2c03181.
[28] S. Kattel, P. Liu, J.G. Chen, Tuning Selectivity of CO_2 Hydrogenation Reactions at the Metal/Oxide Interface, J. Am. Chem. Soc. 139 (2017) 9739-9754. https://doi.org/10.1021/jacs.7b05362.
[29] J. Li, Y. Lin, X. Pan, D. Miao, D. Ding, Y. Cui, J. Dong, X. Bao, Enhanced CO_2 Methanation Activity of Ni/Anatase Catalyst by Tuning Strong Metal–Support Interactions, ACS Catal. 9 (2019) 6342-6348. https://doi.org/10.1021/acscatal.9b00401.
[30] W.L. Vrijburg, E. Moioli, W. Chen, M. Zhang, B.J.P. Terlingen, B. Zijlstra, I.A.W. Filot, A. Züttel, E.A. Pidko, E.J.M. Hensen, Efficient Base-Metal NiMn/TiO_2 Catalyst for CO_2 Methanation, ACS Catal. 9 (2019) 7823-7839. https://doi.org/10.1021/acscatal.9b01968.
[31] S. Li, J. Gong, Strategies for Improving the Performance and Stability of Ni-based Catalysts for Reforming Reactions, Chem. Soc. Rev. 43 (2014) 7245-7256. https://doi.org/10.1039/C4CS00223G.
[32] J.-y. Jing, Z.-h. Wei, Y.-b. Zhang, H.-c. Bai, W.-y. Li, Carbon Dioxide Reforming of Methane over MgO-Promoted Ni/SiO_2 Catalysts with Tunable Ni Particle Size, Catal. Today 356 (2020) 589-596. https://doi.org/10.1016/j.cattod.2020.01.006.
[33] L. Xu, F. Wang, M. Chen, H. Yang, D. Nie, L. Qi, X. Lian, Alkaline-Promoted Ni based Ordered Mesoporous Catalysts with Enhanced Low-Temperature Catalytic Activity Toward CO_2 Methanation, RSC Adv. 7 (2017) 18199-18210. https://doi.org/10.1039/c7ra01673e.
[34] M.-M. Millet, A.V. Tarasov, F. Girgsdies, G. Algara-Siller, R. Schlögl, E. Frei, Highly Dispersed Ni_0/$Ni_xMg_{1-x}O$ Catalysts Derived from Solid Solutions: How Metal and Support Control the CO_2 Hydrogenation, ACS Catal. 9 (2019) 8534-8546. https://doi.org/10.1021/acscatal.9b02332.
[35] M.M. Millet, G. Algara-Siller, S. Wrabetz, A. Mazheika, F. Girgsdies, D. Teschner, F. Seitz, A. Tarasov, S.V. Levchenko, R. Schlogl, E. Frei, Ni Single Atom Catalysts for CO_2 Activation, J. Am. Chem. Soc. 141 (2019) 2451-2461. https://doi.org/10.1021/jacs.8b11729.
[36] W. Zhang, T. Pu, Z. Wang, L. Shen, M. Zhu, Combined In Situ Diffuse Reflectance Infrared Fourier Transform Spectroscopy and Kinetic Studies on CO_2 Methanation Reaction over Ni/Al_2O_3, Ind. Eng. Chem. Res. 61 (2022) 9678-9685. https://doi.org/10.1021/acs.iecr.2c01343.
[37] J. Huang, X. Li, X. Wang, X. Fang, H. Wang, X. Xu, New Insights into CO_2 Methanation Mechanisms on Ni/MgO Catalysts by DFT Calculations: Elucidating Ni and MgO Roles and Support Effects, J. CO2 Util. 33 (2019) 55-63. https://doi.org/10.1016/j.jcou.2019.04.022.
[38] J. Ren, H. Guo, J. Yang, Z. Qin, J. Lin, Z. Li, Insights into the Mechanisms of CO_2 Methanation on Ni(111) Surfaces by Density Functional Theory, Appl. Surf. Sci. 351 (2015) 504-516. https://doi.org/10.1016/j.apsusc.2015.05.173.
[39] P. Lozano-Reis, H. Prats, P. Gamallo, F. Illas, R. Sayós, Multiscale Study of the Mechanism of Catalytic CO_2 Hydrogenation: Role of the Ni(111) Facets, ACS Catal. 10 (2020) 8077-8089. https://doi.org/10.1021/acscatal.0c01599.
[40] J.-N. Park, E.W. McFarland, A Highly Dispersed Pd–Mg/SiO_2 Catalyst Active for Methanation of CO_2, J. Catal. 266 (2009) 92-97. https://doi.org/10.1016/j.jcat.2009.05.018.

[41] P. Hongmanorom, J. Ashok, G. Zhang, Z. Bian, M.H. Wai, Y. Zeng, S. Xi, A. Borgna, S. Kawi, Enhanced Performance and Selectivity of CO_2 Methanation over Phyllosilicate Structure Derived Ni-Mg/SBA-15 Catalysts, Appl. Catal. B 282 (2021) 119564. https://doi.org/10.1016/j.apcatb.2020.119564.

[42] P. Hongmanorom, J. Ashok, P. Chirawatkul, S. Kawi, Interfacial Synergistic Catalysis over Ni Nanoparticles Encapsulated in Mesoporous Ceria for CO_2 Methanation, Appl. Catal. B 297 (2021) 120454. https://doi.org/10.1016/j.apcatb.2021.120454.

[43] B. Yan, B. Zhao, S. Kattel, Q. Wu, S. Yao, D. Su, J.G. Chen, Tuning CO_2 Hydrogenation Selectivity via Metal-Oxide Interfacial Sites, J. Catal. 374 (2019) 60-71. https://doi.org/10.1016/j.jcat.2019.04.036.

[44] C. La Fontaine, S. Belin, L. Barthe, O. Roudenko, V. Briois, ROCK: A Beamline Tailored for Catalysis and Energy-Related Materials from ms Time Resolution to µm Spatial Resolution, Synchrotron Radiation News 33 (2020) 20-25. https://doi.org/10.1080/08940886.2020.1701372.

[45] V. Briois, C. La Fontaine, S. Belin, L. Barthe, T. Moreno, V. Pinty, A. Carcy, R. Girardot, E. Fonda, ROCK: the new Quick-EXAFS beamline at SOLEIL, Journal of Physics: Conference Series 712 (2016) 012149. https://doi.org/10.1088/1742-6596/712/1/012149.

[46] E. Fonda, A. Rochet, M. Ribbens, L. Barthe, S. Belin, V. Briois, The SAMBA quick-EXAFS monochromator: XAS with edge jumping, Journal of Synchrotron Radiation 19 (2012) 417-424. https://doi.org/10.1107/S0909049512009703.

[47] C. Lesage, E. Devers, C. Legens, G. Fernandes, O. Roudenko, V. Briois, High pressure cell for edge jumping X-ray absorption spectroscopy: Applications to industrial liquid sulfidation of hydrotreatment catalysts, Catal. Today 336 (2019) 63-73. https://doi.org/10.1016/j.cattod.2019.01.081.

[48] B. Ravel, M. Newville, ATHENA, ARTEMIS, HEPHAESTUS: data analysis for X-ray absorption spectroscopy using IFEFFIT, Journal of Synchrotron Radiation 12 (2005) 537-541. https://doi.org/10.1107/S0909049505012719.

[49] J. Jaumot, A. de Juan, R. Tauler, MCR-ALS GUI 2.0: New features and applications, Chemometrics and Intelligent Laboratory Systems 140 (2015) 1-12. https://doi.org/10.1016/j.chemolab.2014.10.003.

[50] J. Jaumot, R. Gargallo, A. de Juan, R. Tauler, A graphical user-friendly interface for MCR-ALS: a new tool for multivariate curve resolution in MATLAB, Chemometrics and Intelligent Laboratory Systems 76 (2005) 101-110. https://doi.org/10.1016/j.chemolab.2004.12.007.

[51] J. Tan, J. Wang, Z. Zhang, Z. Ma, L. Wang, Y. Liu, Highly Dispersed and Stable Ni Nanoparticles Confined by MgO on ZrO_2 for CO_2 Methanation, Appl. Surf. Sci. 481 (2019) 1538-1548. https://doi.org/10.1016/j.apsusc.2019.03.217.

[52] M. Guo, G. Lu, The Effect of Impregnation Strategy on Structural Characters and CO_2 Methanation Properties over MgO Modified Ni/SiO2 Catalysts, Catal. Commun. 54 (2014) 55-60. https://doi.org/10.1016/j.catcom.2014.05.022.

[53] F. He, J. Zhuang, B. Lu, X. Liu, J. Zhang, F. Gu, M. Zhu, J. Xu, Z. Zhong, G. Xu, F. Su, Ni-based Catalysts Derived from Ni-Zr-Al Ternary Hydrotalcites Show Outstanding Catalytic Properties for Low-Temperature CO_2 Methanation, Appl. Catal. B 293 (2021) 120218. https://doi.org/10.1016/j.apcatb.2021.120218.

[54] M.-J. Kim, J.-R. Youn, H.J. Kim, M.W. Seo, D. Lee, K.S. Go, K.B. Lee, S.G. Jeon, Effect of Surface Properties Controlled by Ce Addition on CO_2 Methanation over Ni/Ce/Al_2O_3 Catalyst, Int. J. Hydrogen Energy 45 (2020) 24595-24603. https://doi.org/10.1016/j.ijhydene.2020.06.144.

[55] W.L. Vrijburg, G. Garbarino, W. Chen, A. Parastaev, A. Longo, E.A. Pidko, E.J.M. Hensen, Ni-Mn Catalysts on Silica-Modified Alumina for CO_2 Methanation, J. Catal. 382 (2020) 358-371. https://doi.org/10.1016/j.jcat.2019.12.026.
[56] M. Li, H. Amari, A.C. van Veen, Metal-oxide Interaction Enhanced CO_2 Activation in Methanation over Ceria Supported Nickel Nanocrystallites, Appl. Catal. B 239 (2018) 27-35. https://doi.org/10.1016/j.apcatb.2018.07.074.
[57] H.C. Wu, Y.C. Chang, J.H. Wu, J.H. Lin, I.K. Lin, C.S. Chen, Methanation of CO_2 and Reverse Water Gas Shift Reactions on Ni/SiO_2 Catalysts: the Influence of Particle Size on Selectivity and Reaction Pathway, Catal. Sci. Technol. 5 (2015) 4154-4163. https://doi.org/10.1039/c5cy00667h.
[58] J.K. Kesavan, I. Luisetto, S. Tuti, C. Meneghini, G. Iucci, C. Battocchio, S. Mobilio, S. Casciardi, R. Sisto, Nickel Supported on YSZ: The Effect of Ni Particle Size on the Catalytic Activity for CO_2 Methanation, J. CO2 Util. 23 (2018) 200-211. https://doi.org/10.1016/j.jcou.2017.11.015.
[59] A. Khodakov, J. Yang, S. Su, E. Iglesia, A.T. Bell, Structure and properties of vanadium oxide-zirconia catalysts for propane oxidative dehydrogenation, J. Catal. 177 (1998) 343-351. https://doi.org/10.1006/jcat.1998.2143.
[60] T. Pu, L. Shen, X. Liu, X. Cao, J. Xu, I.E. Wachs, M. Zhu, Formation and influence of surface hydroxyls on product selectivity during CO_2 hydrogenation by Ni/SiO_2 catalysts, J. Catal. 400 (2021) 228-233. https://doi.org/10.1016/j.jcat.2021.06.008.
[61] E.B. Sterk, A.E. Nieuwelink, M. Monai, J.N. Louwen, E.T.C. Vogt, I.A.W. Filot, B.M. Weckhuysen, Structure Sensitivity of CO(2) Conversion over Nickel Metal Nanoparticles Explained by Micro-Kinetics Simulations, JACS Au 2 (2022) 2714-2730. 10.1021/jacsau.2c00430.
[62] A. Karelovic, P. Ruiz, Mechanistic Study of Low Temperature CO_2 Methanation over Rh/TiO_2 Catalysts, J. Catal. 301 (2013) 141-153. https://doi.org/10.1016/j.jcat.2013.02.009.
[63] V. De Coster, N.V. Srinath, P. Yazdani, H. Poelman, V.V. Galvita, Does CO_2 Oxidize Ni Catalysts? A Quick X-ray Absorption Spectroscopy Answer, J. Phys. Chem. Lett. 13 (2022) 7947-7952. https://doi.org/10.1021/acs.jpclett.2c01790.
[64] Y. Guo, J. Feng, W. Li, Effect of the Ni size on CH_2/CO_2 reforming over Ni/MgO catalyst: A DFT study, Chin. J. Chem. Eng. 25 (2017) 1442-1448. https://doi.org/10.1016/j.cjche.2017.03.024.
[65] J. Li, E. Croiset, L. Ricardez-Sandoval, Effect of Metal–Support Interface During CH_4 and H_2 Dissociation on Ni/γ-Al_2O_3: A Density Functional Theory Study, J. Phys. Chem. C 117 (2013) 16907-16920. https://doi.org/10.1021/jp402421q.